J. Electrochem. Sci. Eng. **15(4)** (2025) 2726; *http://dx.doi.org/10.5599/jese.2726*

Open Access : : ISSN 1847-9286
www.jESE-online.org

Original scientific paper

Microstructure and electrochemical corrosion behaviour of API 5L X90 pipeline steel in a simulated soil environment

Mahdi Yeganeh✉, Mostafa Eskandari and Hasan Mousavi

Department of Materials Science and Engineering, Faculty of Engineering, Shahid Chamran University of Ahvaz, Iran

Corresponding author: ✉*m.yeganeh@scu.ac.ir; Tel.: +98-61-33226611*

Received: March 24, 2025; Accepted: May 4, 2025; Published: May 7, 2025

Abstract

API 5L X90 pipeline steel, valued for its high strength in oil and gas pipelines, is susceptible to corrosion in aggressive soil environments containing moisture, chlorides, and other corrosive agents. This study aims to investigate the electrochemical corrosion behaviour of this steel in a simulated soil solution to understand its corrosion mechanisms and pipeline durability. The research employs electrochemical techniques, including electrochemical impedance spectroscopy, electrochemical noise and potentiodynamic polarization testing. Microstructural analysis showed that the composition of the steel, consisting of elongated ferrite grains, polygonal ferrite, granular bainite, and small amounts of martensite-austenite (MA), significantly influences its corrosion behaviour. EIS results indicated the presence of multiple time constants due to various oxide films and corrosion products, which hindered the penetration of corrosive species over time. As a result of corrosion products forming on the active sites and rendering them inactive, the charge transfer resistance increased by approximately 1.5 times. Potentiodynamic polarization tests indicated an absence of passivation, accompanied by a decrease in corrosion current density and a shift in corrosion potential toward the cathodic direction during immersion. Surface analysis after 100 hours identified localized corrosion, including cracks and pits, which pose risks to the steel's structural integrity. The findings emphasize the need to understand the corrosion processes and their impact on impedance characteristics, advocating for targeted corrosion prevention and treatment strategies to enhance pipeline longevity and reliability.

Keywords

Near-neutral simulated soil solution; steel pipes; electrochemical corrosion tests; microstructural analysis; surface morphology

Introduction

Crude oil and natural gas are essential raw hydrocarbons used globally for energy. From production to refineries, they are transported *via* pipelines, which play a crucial role in their distribution. High-strength low-alloy (HSLA) steels are favoured for pipeline construction because of their

excellent mechanical properties, good weldability, resistance to corrosion, cost-effectiveness, ease of forming, and wide availability [1-4]. The International Organization for Standardization (ISO) and the American Petroleum Institute (API) set standards for pipeline materials [4]. API standards, widely adopted worldwide, outline specifications for chemical composition and mechanical properties. API 5L categorizes pipes into two product specification levels: PSL 1 and PSL 2. PSL 1 encompasses grades ranging from A25 to X70, whereas PSL 2 includes grades from B to X120. These standards guarantee the quality, reliability, and safety of pipelines, which are essential for the effective transportation of energy resources [5,6].

Corrosion is a naturally occurring process resulting from the interaction between materials and their surrounding environment. This interaction leads to the gradual degradation of the material, structural damage, and ultimately the conversion of valuable products into non-functional waste [7,8]. Corrosion in API pipeline steel predominantly occurs in moist and aqueous environments within oil and gas pipeline infrastructures. Water and aggressive agents such as chlorides, carbon dioxide (CO_2), and hydrogen sulphide (H_2S) significantly accelerate the corrosion rate, endangering pipeline integrity and longevity. Moist conditions facilitate electrochemical reactions, while factors like temperature variations, pH levels, and microbial activity further influence corrosion dynamics. High temperatures accelerate corrosion reactions, acidic environments worsen material degradation, and certain bacteria can induce localized corrosion. Understanding these factors is crucial for developing strategies to mitigate corrosion, ensuring safe and efficient operation of pipelines [9,10].

HSLA steels have emerged as critical materials in the oil and gas industry, particularly for pipeline applications, due to their superior mechanical properties and cost-effectiveness. These steels, including grades such as X70, X80 and X90, offer an optimal balance of strength, toughness, and weldability, making them ideal for high-pressure transmission pipelines. The development of HSLA steels has been driven by the need for materials that can withstand increasingly demanding operational conditions, including higher pressures, more corrosive environments, and extreme temperatures. Despite their advantages, HSLA pipeline steels face significant challenges, especially regarding corrosion resistance in aggressive environments containing chlorides, carbon dioxide, and hydrogen sulphide. The complex microstructure of HSLA steels, typically consisting of fine-grained ferrite with dispersed precipitates, plays a crucial role in determining their corrosion behaviour [11-13].

HSLA steels have been developed to meet the growing global energy demand. These steels are used for oil and gas pipelines due to their high strength and low alloy content. Among these, X90 grade steel has gained prominence due to its exceptional mechanical properties and cost-effectiveness. However, the corrosion of X90 pipeline steel remains a significant concern, potentially compromising the integrity and safety of pipeline infrastructure. There is limited data about the corrosion of X90 pipeline steel in the corrosive soil media. In a study conducted by Luo *et al*. [14], the electrochemical corrosion behaviours of X90 steel were examined in a near-neutral simulated soil solution (NS4). Utilizing a longitudinally submerged arc welding pipe, the research examines the corrosion characteristics of both base metal and welding materials through various electrochemical tests, including open-circuit potential measurements, potentiostatic polarization, and electrochemical impedance spectroscopy. The findings revealed that the base metal exhibits higher corrosion resistance compared to the welding material, with polarization time significantly influencing corrosion resistance and current density.

In another work, Luo *et al.* [15] found no activation-passivation phenomenon for X90 steel. Stress corrosion cracking (SCC) sensitivity indicators decrease initially and increase with more negative applied potentials. Hydrogen embrittlement plays a more significant role at higher negative

potentials of -1000 and -1200 mV. Besides, the mechanisms of SCC were anodic dissolution and hydrogen embrittlement, varying by the applied potential.

Another work accomplished by Bi *et al*. [16] presents a method to monitor uniform corrosion in X90 steel pipelines. It uses acoustic emission (AE) and electrochemical techniques to categorize the corrosion process into three stages: initial metal dissolution, corrosion product accumulation, and corrosion stabilization, with each stage characterized by distinct AE signal patterns. This approach offers a practical, non-destructive tool for assessing pipeline integrity in real-time, which can be valuable for maintenance strategies.

Some studies focus on the corrosion of high-strength low-alloy (HSLA) steels, specifically API 5L X90, in aggressive soil environments. These environments, characterized by moisture, chlorides, carbon dioxide, and hydrogen sulphide, can accelerate material degradation, threatening pipeline integrity. The literature notes that despite the excellent mechanical properties and cost-effectiveness of X90 steel, its corrosion resistance in such conditions is a concern, with limited data available. This gap underscores the urgency of the investigation to inform strategies that mitigate corrosion and ensure pipeline safety.

Given these corrosion challenges, it is imperative to thoroughly investigate the electrochemical behaviour of API X90 steel in a simulated soil environment. Advanced techniques such as potentiodynamic polarization, electrochemical impedance spectroscopy (EIS), and electrochemical noise analysis provide critical insights into corrosion mechanisms and rates. Furthermore, techniques such as scanning electron microscopy (SEM) and energy-dispersive X-ray spectroscopy (EDS) are instrumental in identifying microstructural characteristics that affect corrosion resistance. Understanding the corrosion mechanisms of X90 steel is essential for the development of effective prevention strategies and enhancing the durability of pipeline systems. Consequently, this research seeks to examine the electrochemical performance of X90 steel under simulated soil solution conditions.

Experimental

In this research, X90 pipeline steel plates with a thickness of 10 mm were employed. The chemical composition of the alloy is detailed in Table 1. Similarly, the composition of the soil NS4 solution [15] in the experiments is outlined in Table 2.

Table 1. *Elemental composition of X90 pipeline steel*

	Content, wt. %													
Fe	C	Si	Mn	Cr	Mo	Ni	Nb	Ti	Cu	Al	V	Co	S	P
Base	0.05	0.25	1.45	0.131	0.09	0.133	0.041	0.015	0.102	0.03	0.027	0.003	<0.001	0.12

Table 2*. Chemical composition of simulated soil solution in this study (pH≈7.3)*

	KCl	$CaCl_2 \cdot 2H_2O$	$MgSO_4 \cdot 7H_2O$	$NaHCO_3$
Content, g l^{-1}	0.122	0.181	0.131	0.483

The X90 alloy specimens were prepared to ensure precise experimental findings. They were first carefully polished using silicon carbide sandpaper until they had a 3000-grit texture that was smooth. After that, acetone and water were used to thoroughly wash the specimens to remove any remaining pollutants. In order to prepare them for electrochemical testing, the cleaned samples were then embedded in epoxy resin and wired to a copper rod. The specimens were etched by immersion in a 2 % nital solution in preparation for electron and optical microscopy examinations. An optical microscope (Meijitechno IM7200, Japan) and a field emission scanning electron microscope (Mira3

Model, Czech Republic) were used to analyse the surfaces. X-ray diffraction (XRD) was performed using an X'Pert Pro MPD diffractometer (Malvern Panalytica, The Netherlands) to evaluate the composition of X90 in the 2θ range of 20 to 80° using a CuKα (λ = 0.15406 nm) radiation.

A three-electrode cell design was used for the electrochemical corrosion tests, with the sample under investigation serving as the working electrode. A 1 cm^2 exposed region was submerged at room temperature in a simulated soil solution. A platinum wire counter electrode and an Ag/AgCl, (3 M KCl) reference electrode were used for electrochemical measurements, which were controlled by NOVA 2.1 software *via* an Autolab PGSTAT 302 potentiostat-galvanostat (Metrohm AG, Switzerland). ZView software was employed to calculate corrosion parameters using an equivalent circuit fitting. Before the first test, the sample was immersed in the solution for 1 h to stabilize the electrochemical reactions. Electrochemical impedance spectroscopy (EIS) at open circuit potential (OCP) was performed with 5 mV alternating current (AC) signal over the frequency range of 10 kHz to 10 mHz. A scan rate of 1 mV s^{-1} for potentiodynamic polarization studies provided important electrochemical parameters in the solution. Tafel extrapolation was used to measure the corrosion current density (j_{corr}), corrosion potential (E_{corr}), corrosion rate (CR), and both the cathodic and anodic slopes (β_c and β_a) after the potential was scanned from -200 to +800 mV relative to Ag/AgCl. Furthermore, two identical X90 working electrodes and an Ag/AgCl reference electrode with an equal distance between the working electrodes were used to conduct electrochemical noise (EN) analysis in the NS4 solution. Power spectral density (PSD) plots were produced by applying a Hann window function after the time-domain potential and current noise data were obtained and a fast Fourier transform (FFT) was used to convert the data to the frequency domain [17,18]. To ensure the reproducibility of the data, each electrochemical test was conducted at least three times. Triplicate measurements were performed on fresh surfaces to confirm the consistency of the results. All electrochemical tests were conducted at 25 °C. Additionally, the tests were carried out at varying immersion times of 1, 20 and 100 hours.

Results and discussion

Figures 1(a) and (b) illustrate the optical and FESEM micrographs of X90 steel, respectively. Figure 1(a) shows a microstructure consisting of elongated and densely packed ferrite grains resulting from the rolling process, along with some equiaxed and polygonal ferritic grains. The FESEM analysis of X90 revealed a banded microstructure composed of different phases. This banded pattern is characteristic of pipeline steels and is attributed to the thermomechanical processing during fabrication. The microstructure consists of polygonal ferrite and granular bainite (the darker matrix), with a minor presence of martensite-austenite (MA) constituents (the brighter phase) in Figure 1(b). This intricate composition reflects the complex thermomechanical history and the balance of phases contributing to the overall mechanical properties of the X90 steel. Orientation microscopy was employed to measure the average grain size of the α-phase grains, yielding an average size of 6.5 µm. M/A (martensite/austenite) constituents form during the cooling of high-strength pipeline steels when carbon-enriched retained austenite partially transforms to martensite. This process is influenced by micro-alloying elements like Nb, cooling rates, and prior austenite grain size. Rapid cooling and austenite decomposition kinetics promote carbon stabilization in residual austenite, leading to M/A islands or elongated particles. These constituents critically impact mechanical properties, such as fracture toughness, depending on their size, morphology, and distribution within the microstructure [19].

The XRD analysis of the X90 pipeline steel, as shown in Figure 2, revealed the presence of ferrite (α-Fe) as the primary phase. This is indicated by the prominent diffraction peaks corresponding to the (110) and (200) planes of the body-cantered cubic (BCC) structure.

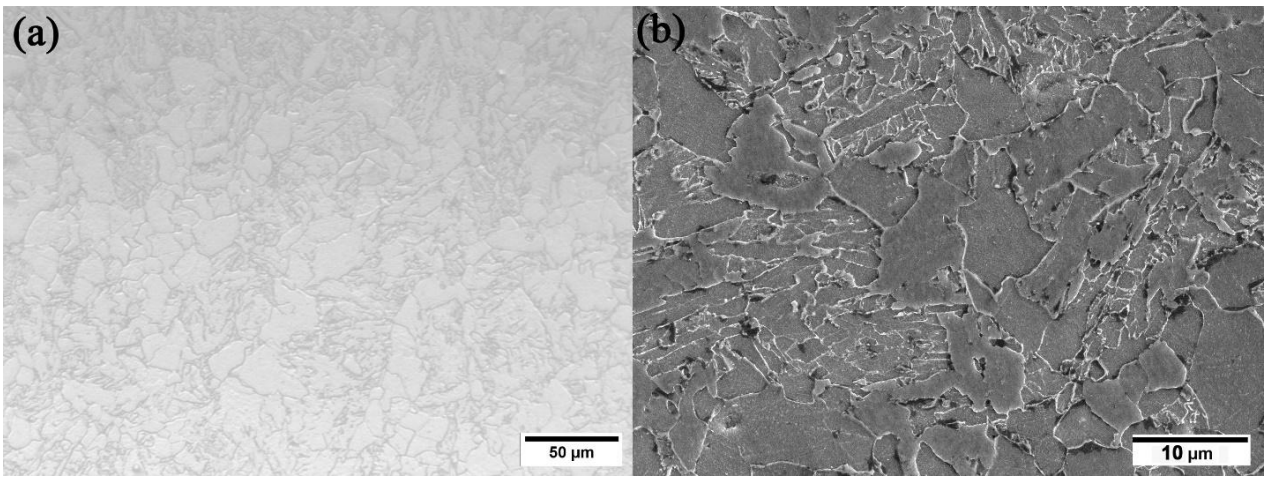

Figure 1. *(a) Optical micrograph and (b) FESEM micrograph of X90 pipeline steel*

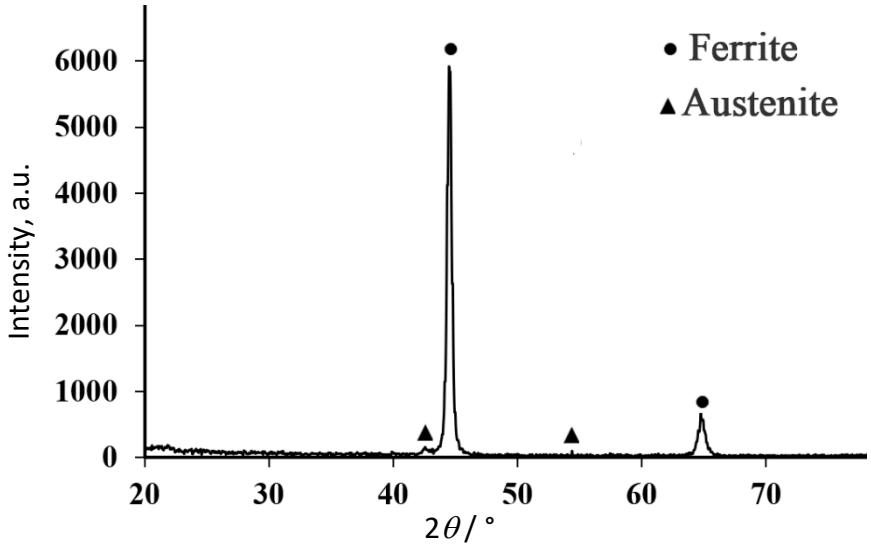

Figure 2. *XRD pattern of X90 pipeline steel*

However, two other peaks are associated with the presence of austenite (γ-Fe). The volume fraction of retained austenite in the base metal was quantified to be about 2 % according to the Rietveld method, indicating a predominantly ferritic microstructure with minimal austenitic phase. The incorporation of a secondary phase into steel adversely impacts its corrosion resistance due to the differences in the free energy of the resulting phases [20,21].

The Nyquist plots in Figure 3 for X90 pipeline steel in the simulated soil solution display the depressed capacitive semi-circles, indicating the interplay of charge transfer and oxide layer behaviours. The diameter of the Nyquist plot semi-circle directly indicates charge transfer resistance; alloys with larger semi-circle diameters in electrolyte solution show higher resistance values, reflecting enhanced corrosion inhibition performance due to a lower rate of charge transfer reactions that facilitate corrosion [22]. These plots show an increasing charge transfer resistance with immersion time, indicating the formation and growth of corrosion products. At 100 hours, the corrosion product layer is well-formed and provides better protection, as evidenced by the larger semicircular arc. The equivalent circuits associated with immersion times of 1, 20 and 100 hours, reflecting the stages of corrosion product formation and their protective nature, are shown in Figures 4(a) to 4(c), respectively.

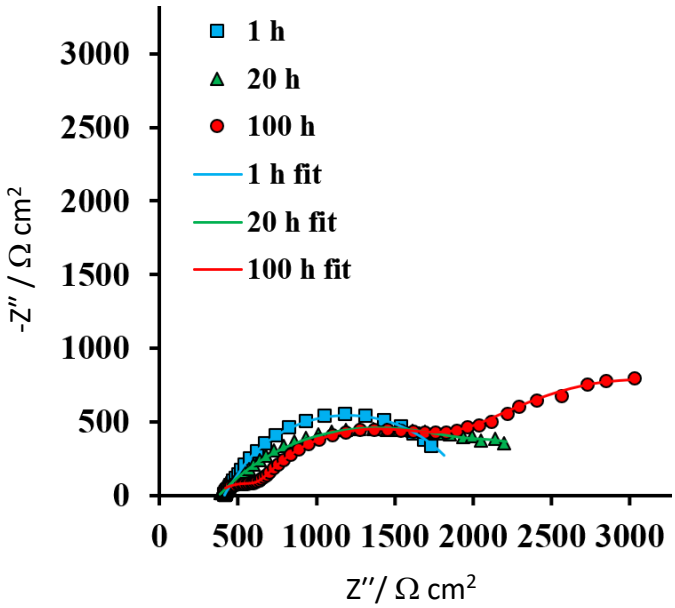

***Figure 3**. Nyquist plots of the X90 pipeline steel after immersing in a simulated soil solution for 1, 20, and 100 hours*

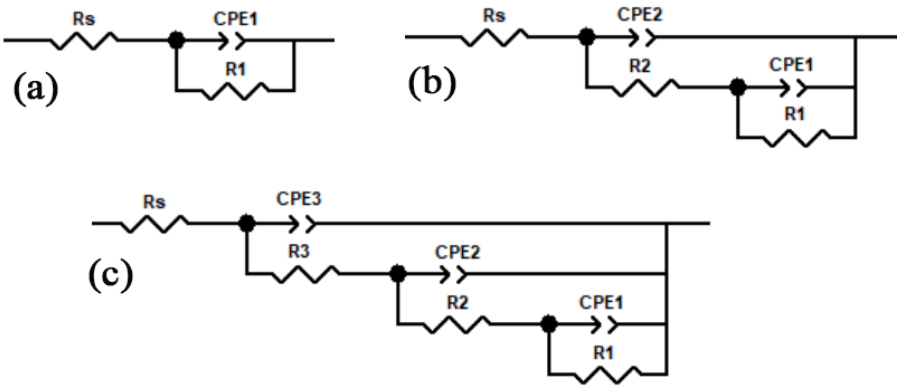

***Figure 4.** Different equivalent circuits regarding the corrosion process of X90 pipeline steel at (a) 1 h, (b) 20 h and (c) 100 h of immersion in the simulated soil solution*

Each circuit includes resistors (R) and constant phase elements (CPE), which are used to model the electrochemical impedance of the system. For example, at 100 h of immersion, the corrosion behaviour in this alloy involves several components: solution resistance (R_s), resistance of the outer scattered porous film (R_3), and its corresponding constant phase element (CPE_3) at high frequencies. At lower frequencies, the second time constant includes the resistance of the inner oxide film (R_2) and its associated CPE_2. Additionally, R_1 and CPE_1 represent the charge transfer phenomenon. The charge transfer resistance (R_{ct}) can be determined from the Nyquist plot by examining the point at which the real part of the impedance (Z') approaches zero [23,24]. This condition allows for the precise determination of the charge transfer resistance, a critical parameter in evaluating electrochemical systems and efficiency. Constant phase elements (CPEs) demonstrate non-ideal behaviour in contrast to ideal capacitors. Using $Z_{CPE}=Q^{-1}(j\omega)^{-n}$, the impedance expression for the CPE (Z_{CPE}) may be computed. Here, $j^2 = -1$, ω is the angular frequency, and n is an exponential factor of CPE with a value between 0 and 1. When $n = 1$, the CPE displays entirely capacitive behaviour and shows a perfectly flat surface. The CPE acts as a resistor at $n = 0$, and corresponds to Warburg impedance at $n = 0.5$ [25-28]. A constant phase element (CPE) is used instead of an ideal capacitor due to surface imperfections, roughness, or flaws on the electrode [22,29,30].

Upon 1 hour of immersion, the X90 alloy surface remains largely unaltered, displaying a single time constant attributable to the corrosion mechanism, with R_1 representing the charge transfer resistance, which indicates the corrosion rate. After immersion of 20 hours, a second time constant (CPE_2 and R_2) emerges, likely due to the development of initial corrosion products and an increase in surface oxygen enrichment. This development suggests a nascent corrosion product layer that moderately impedes the ingress of corrosive species. Finally, at 100 hours of immersion, a third time constant (CPE_3 and R_3) becomes evident, potentially signifying the formation of diverse and scattered corrosion products characterized by low corrosion resistance, possibly due to the adsorption of electrolyte components onto the alloy surface. These observations collectively illustrate the dynamic evolution of the corrosion process and the corresponding impact on the impedance characteristics of the X90 alloy over time.

The fitting results from electrochemical impedance spectroscopy (EIS) shown in Table 3 exhibit an excellent match with the experimental data, with χ^2 values less than 0.002. The data demonstrate that the charge transfer resistance (R_1) of the X90 alloy increases steadily from 1575 to 2393 Ω cm² as time progresses. This indicates that the corrosion process is being hindered by the development of corrosion products on the surface. Additionally, as time progresses, two more time constants (2 and 3) appear at the interface, associated with the development of various oxide films. Towards the end of the immersion period, a time constant with a resistance of 292 Ω cm^2 emerges, likely linked to the adsorption of electrolytic species on the surface, a topic to be discussed further. In the mid-frequency range, another time constant with a resistance of 1338 Ω cm^2 may be related to the formation of additional protective oxide films on the surface of the alloy. The electrochemical potential disparity between the present phases (ferrite and M/A phases in X90 pipeline steel) adds an extra driving force, leading to a more rapid degradation of the steel surface by dissolved ions or atoms. However, the weak anodic zones (M/A in the grain boundaries) can be covered by corrosion products over time, and the corrosion process can be mitigated.

Additionally, Equation (1) enables the calculation of the double layer capacitance (C_{dl}) of the film by utilizing data obtained from the constant phase element. This provides valuable information about the charge storage capacity, which is crucial for influencing corrosion resistance [27,31]:

$$C_{dl}=Q_{dl}^{\frac{1}{n_{ct}}}R_s^{\frac{1-n_{ct}}{n_{ct}}} \quad (1)$$

The values of R_s, Q_{dl} (CPE_1), and n_{ct} (n_1) may be found in Table 2. The values of C_{dl} after 1, 20 and 100 hours of immersion were calculated as 101, 30 and 25 μF cm^{-2}, respectively, demonstrating a time-dependent reduction in the electrochemical activity of the electrical double layer. In addition, the sum of R_1, R_2 and R_3 can be defined as polarization resistance (R_p), which is critical for controlling the rate of corrosion reactions at the metal-solution interface [22]. A higher R_p value indicates a slower reaction rate, often reflecting enhanced corrosion resistance for the X90 alloy. The values of R_p for immersion times of 1, 20, and 100 hours are approximately 1575, 2207 and 4023 Ω cm², respectively.

Table 3*. The electrochemical impedance parameters acquired through ZView simulation for the X90 pipeline*

Time, h	R_s / Ω cm^2	R_1 / Ω cm^2	Q_1 / μF cm^{-2} s^{n-1}	n_1	R_2 / Ω cm^2	Q_2 / μF cm^{-2} s^{n-1}	n_2	R_3 / Ω cm^2	Q_3 / μF cm^{-2} s^{n-1}	n_3	χ^2
1	415	1575	217	0.76	-	-	-	-	-	-	0.001
20	380	1890	230	0.55	317	105	0.7	-	-	-	0.002
100	370	2393	150	0.68	1338	130	0.71	292	18	0.6	0.001

Figure 5 depicts the Bode spectra related to the corrosion of X90 samples. The high-frequency parts of the spectra reveal the barrier properties of the rust products, whereas the part of the spectra at low frequencies depicts the corrosion processes occurring at the oxide/X90 alloy interface. The Bode impedance spectra for X90, when measured in the simulated soil solution, exhibit primarily resistive characteristics at low frequencies (ranging from 10^{-2} to 10^{-1} Hz). This behaviour transitions to capacitive at intermediate frequencies (from 10^{-1} to 10^{2} Hz) and then reverts to resistive behaviour at higher frequencies (ranging from 10^{2} to 10^{4} Hz) [32,33]. Notably, after 100 hours of immersion, the sample exhibits a higher impedance compared to other time points, suggesting enhanced corrosion resistance with increasing immersion time. After 1 hour of immersion, a single peak was observed at about 1.5 Hz, indicating a single time constant related solely to the corrosion process. After 20 hours of immersion, the phase plot showed two peaks at 5 and 0.04 Hz, due to the presence of a corrosion product film. Finally, after 100 hours of immersion, at frequencies of 1840, 2.8, and 0.02 Hz, there are three peaks related to the loose corrosion product, protective corrosion product, and charge transfer resistance. On the other hand, the Bode plots show an increase in the impedance modulus, especially at 100 h of immersion, suggesting better surface performance over time.

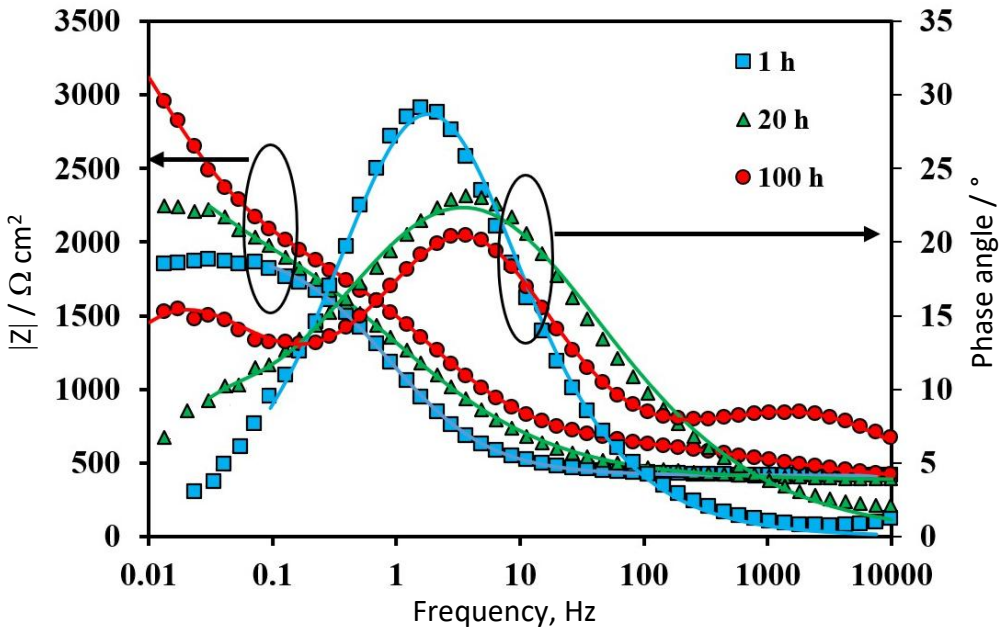

Figure 5. *Bode diagrams of X90 pipeline steel in the simulated soil solution at various immersion times*

The power spectral density (PSD) of the measured current for the X90 alloy in simulated soil solutions at 1, 20 and 100 h is illustrated in Figure 6. The power spectral density (PSD) in electrochemical noise characterizes the distribution of signal power (voltage or current fluctuations) across frequency domains, derived via Fourier transform analysis. A lower current PSD denotes superior corrosion resistance, due to the presence of surface corrosion products after 100 h of immersion [17,34,35]. Significantly, the higher noise level seen at 20 h of immersion, as opposed to 1 h, suggests that the production of protective corrosion products on the X90 surface is not yet complete at this stage. At 100 h of immersion, the significant decrease in noise level validates the correlation between reduced electrochemical activity and enhanced corrosion resistance. The low and stable noise level at 100 h indicates a mature layer, providing effective protection against further corrosion.

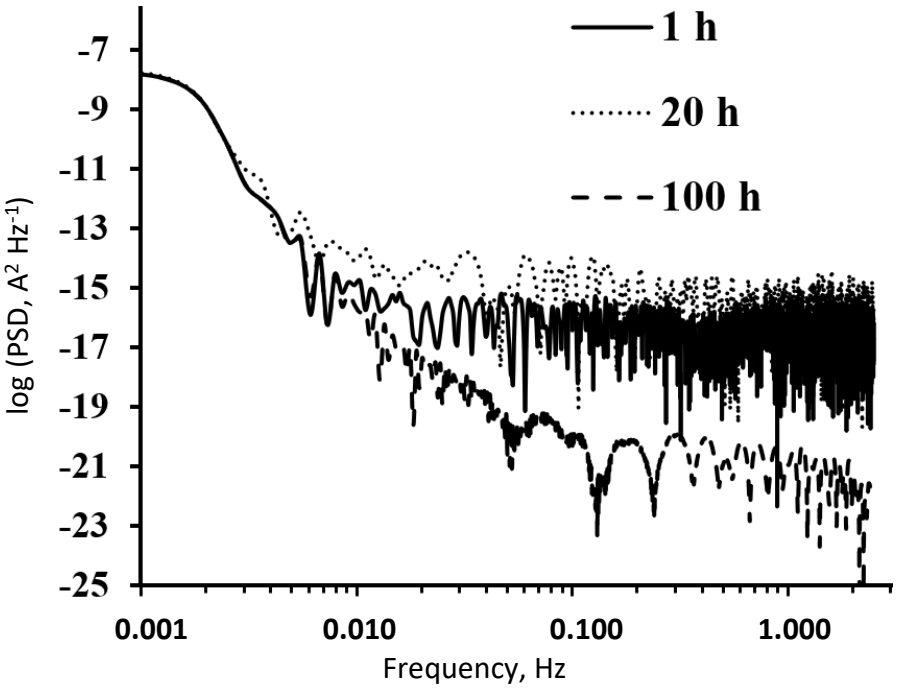

Figure 6. *Electrochemical noise power spectral density (PSD) of X90 pipeline steel over time*

Figure 7 presents the potentiodynamic polarization plots for X90 over various time intervals. Table 4 provides comprehensive details regarding the corrosion performance. The polarization curves provide important electrochemical data such as the corrosion potential (E_{corr}), current density (j_{corr}), Tafel slopes (β_c and β_a), and the corrosion rate (CR; mm year^{-1}).

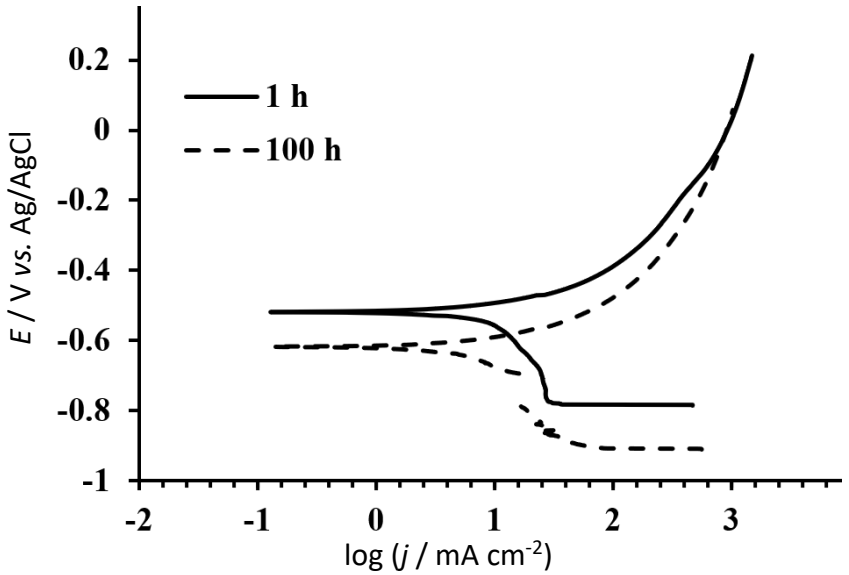

Figure 7. *Potentiodynamic polarization plots of X90 pipeline steel in the simulated soil solution*

Table 4. *Electrochemical corrosion data extracted from the potentiodynamic polarization graphs of X90*

Time, h	E_{corr} / mV *vs.* Ag/AgCl	j_{corr} / μA cm^{-2}	$-\beta_c$ / mV dec^{-1}	$-\beta_a$ / mV dec^{-1}	CR, mm year^{-1}
1	-620	17.3	352	300	0.20
100	-718	10.4	169	307	0.12

The examination of the slopes of the anodic and cathodic branches indicates that the corrosion process is predominantly influenced by the anodic reaction. The curve illustrates characteristics of anodic dissolution, with no evidence of passivation [14]. In other words, as the polarization potential

increases, the anode current density also rises. This indicates that a passivation film does not form during the anodic dissolution process. As can be seen in Table 4, corrosion current density (j_{corr}) of X90 alloy reduces from 17.3 to 10.4 μA cm^{-2} after 100 h of immersion, implying the influence of surface corrosion products. On the other hand, E_{corr} of X90 alloy shifts to a more cathodic direction and decreases from -620 to -718 mV *vs*. Ag/AgCl.

The corrosion rate of X90 alloy can be quantified using Equation (2), as outlined in ASTM Standard G 102-89 [22,36]:

$$\mathrm{CR} = \frac{k\left(EW_{\mathrm{Fe}}\, j_{\mathrm{corr}}\right)}{d_{\mathrm{Fe}}} \tag{2}$$

where k = 3.27×10^{-3} mm g μA^{-1} cm^{-1} year^{-1}, EW is equivalent weight of Fe (about 28); d = 7.87 g cm^{-3} is specific density of Fe and j_{corr} / μA cm^{-2} is estimated using the extrapolation method from the polarization curves [37]. The corrosion rates of X90 alloy after 1 and 100 hours of immersion are 0.2 and 0.12 mm year^{-1}, respectively. These rates may be acceptable in some highly corrosive environments or for certain short-lived components, implying the need for complementary corrosion protection methods, including coating and cathodic protection.

Figures 8(a) and 8(b) display secondary electron micrographs of X90 steel after 100 hours of exposure, magnified at 200× and 500×, respectively. At 200× magnification (Figure 8(a)), the surface appears relatively uniform, with visible cracks and pits signaling localized corrosion. Martensite-austenite (M/A) islands are located at the grain boundaries of the polygonal ferrite (PF) phase, and the potential difference between the M/A and PF phases led to the corrosion of the M/A islands [38]. The potential of M/A islands is significantly greater than that of bainitic ferrite lath structures. This means that M/A islands exhibit enhanced properties or performance qualities that surpass the capabilities of bainitic ferrite lath. Additionally, it is important to note that the corrosion observed in these materials primarily results from the dissolution of ferrite [21]. Therefore, the formation of pits and cracks is facilitated at these ferrite sites. Ferrite, being more anodic due to its lower electrochemical potential, corrodes preferentially compared to bainite, which acts as a cathode in micro-galvanic couple. The 500× magnification micrograph (Figure 8(b)) provides a closer look, revealing finer details such as small pits and corrosion products, indicating more severe degradation. This localized corrosion suggests significant risks to the structural integrity of the X90 pipeline steel, warranting further investigation to determine its impact on mechanical properties and develop effective mitigation strategies.

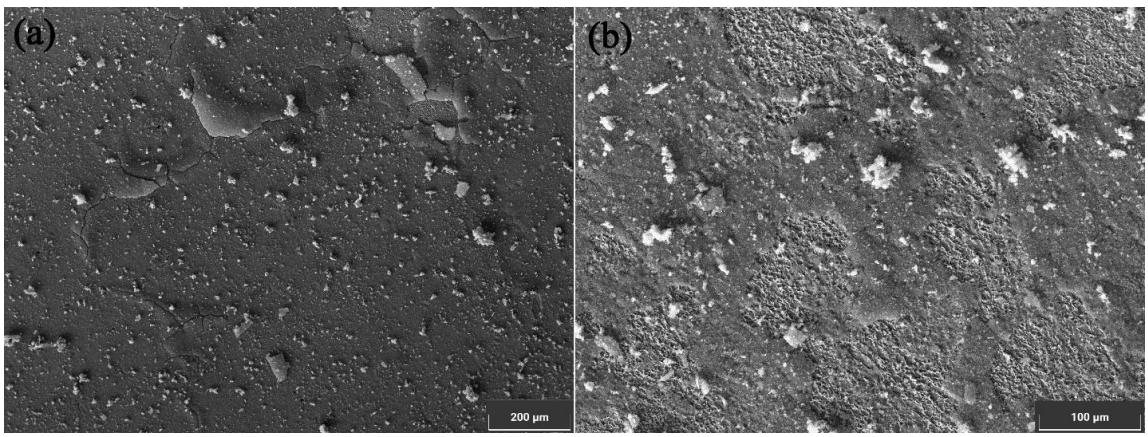

Figure 8. *FESEM micrographs of X90 alloy after 100 h immersion in the simulated soil solution at different magnifications: (a) 200× and (b) 500×*

Figures 9(a) and 9(b) highlight various corrosion regions labeled A, B, and C, along with their respective X-ray energy dispersive spectroscopy (EDS) compositions, as detailed in Table 5. Point A exhibits the highest oxygen content and the least amount of iron content, while point C demonstrates the highest iron content and the lowest oxygen level. This suggests that point C is in the early stages of corrosion due to low oxygen content, while point A is in a more severe stage of corrosion, where oxygen content has increased. Over time, corrosion products can accumulate in anodic regions, effectively altering their characteristics and making them more inert. Consequently, this transformation can cause previously cathodic areas to become anodic relative to the oxide layer. As a result, the distribution of oxide products can extend across the entire surface.

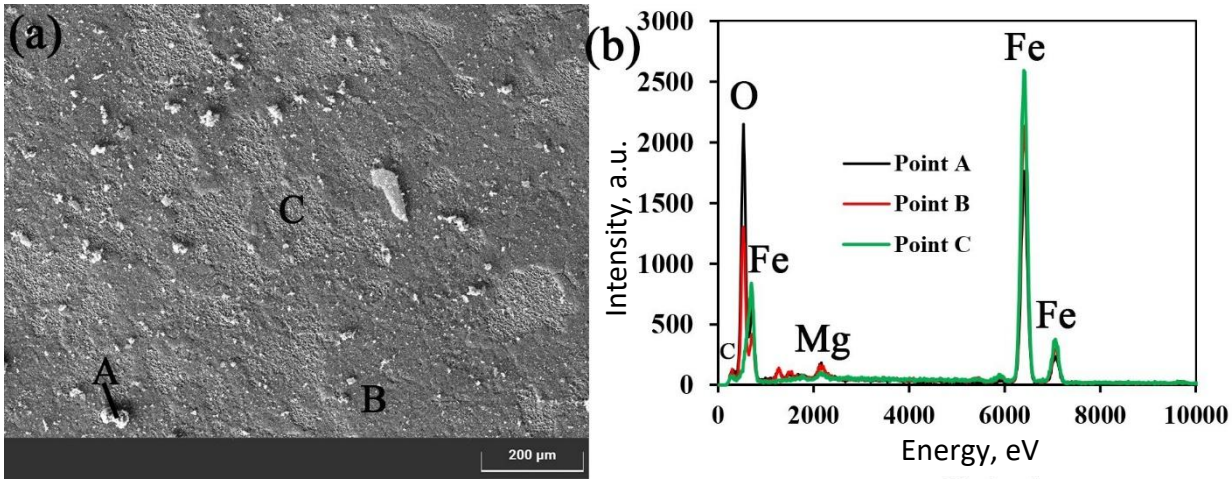

Figure 9. *(a) SEM micrograph and (b) EDS spectrum of specified points (A, B, C)*

Table 5. *Elemental composition of specified points in Figure 9(a)*

Point	Content, wt.%			
	Fe	O	C	Other elements (Mg, Al, Mn)
A	44.4	32.64	18.15	4.81
B	48.12	28.68	18.85	4.35
C	75.36	5.18	17.64	1.82

Conclusions

In a simulated soil solution, the electrochemical corrosion properties of API 5L X90 pipeline steel were investigated in detail. This study included different techniques such as potentiodynamic polarization testing, electrochemical noise, and electrochemical impedance spectroscopy. Micro-structural analysis revealed that the X90 steel consists of elongated ferrite grains, polygonal ferrite, granular bainite, and minor martensite-austenite constituents. These microstructural features significantly influence the corrosion behaviour of the steel. The EIS fitting results indicated the development of multiple time constants associated with the formation of various oxide films and corrosion products, which moderately impeded the ingress of corrosive species over time. Potentiodynamic polarization measurements further confirmed the absence of passivation, with the corrosion current density decreasing and the corrosion potential shifting in the cathodic direction over the immersion period. Surface examination after 100 hours revealed localized corrosion, including cracks and pits, which pose significant risks to the structural integrity of the pipeline steel. Future research should focus on developing tailored coatings for specific soil conditions and exploring alloying strategies to further improve the steel performance, ensuring comprehensive protection and longevity of pipeline infrastructures.

***Acknowledgements**: This study received financial backing from Shahid Chamran University of Ahvaz under Grant Number SCU.EM1403.31395.*

References

[1] U. Bharatiya, P. Gal, A. Agrawal, M. Shah, A. Sircar, *Effect of Corrosion on Crude Oil and* Natural Gas Pipeline with Emphasis on Prevention by Ecofriendly Corrosion Inhibitors, *Journal of Bio- and Tribo-Corrosion* **5** (2019) 35. https://doi.org/10.1007/s40735-019-0225-9

[2] A. Golchinvafa, S.H. Mousavi Anijdan, M. Sabzi, M. Sadeghi, The effect of natural inhibitor concentration of Fumaria officinalis and temperature on corrosion protection mechanism in API X80 pipeline steel in 1 M H_2SO_4 solution, *International Journal of Pressure Vessels and Piping* **188** (2020) 104241. https://doi.org/10.1016/j.ijpvp.2020.104241

[3] R. Branco, F. Berto, Mechanical Behavior of High-Strength, Low-Alloy Steels, *Metals (Basel)* **8** (2018) 610. https://doi.org/10.3390/met8080610

[4] M. Yeganeh, Y. Heydarie, Z. Shahryari, N. Asadi, H. Kahkesh, H. Ramezanalizadeh, Corrosion Inhibitor of API Pipeline Steels, *Journal of Bio- and Tribo-Corrosion* **11** (2025) 44. https://doi.org/10.1007/s40735-025-00965-2

[5] F. Kolawole, S.K.K. Kolawole, J. Agunsoye, J. Adebisi, S. Bello, S. Hassan, Mitigation of Corrosion Problems in API 5L Steel Pipeline, *Journal of Materials and Environmental Science* **9** (2018) 2397-2410. https://www.jmaterenvironsci.com/Document/vol9/vol9_N8/264-JMES-2611-Kolawole.pdf

[6] S. K. Sharma, S. Maheshwari, A review on welding of high strength oil and gas pipeline steels, *Journal of Natural Gas Science and Engineering* **38** (2017) 203-217. https://doi.org/10.1016/j.jngse.2016.12.039

[7] J. Enani, Corrosion control in oil and gas pipeline, *Pipeline Gas Journal* **7** (2016) 1161-1164. https://www.scribd.com/document/361624759/Corrosion-Control-in-Oil-and-Gas-Pipelines

[8] L. M. Alcantar-Martínez, P. A. Ruiz-Trabolsi, R. Tadeo-Rosas, Improving the Surface Properties of an API 5L Grade B Pipeline Steel by Applying the Boriding Process. Part I: Kinetics and Layer Characterization, *Coatings* **13** (2023) 298. https://doi.org/10.3390/coatings13020298

[9] M. Nnoka, T.A. Jack, J. Szpunar, Effects of different microstructural parameters on the corrosion and cracking resistance of pipeline steels, *Engineering Failure Analysis* **159** (2024) 108065. https://doi.org/10.1016/j.engfailanal.2024.108065

[10] X. Wang, D. Wang, C. Deng, C. Li, Effect of H_2S Corrosion on the Fracture Toughness of the X80 Pipeline Steel Welded Joint, *Materials (Basel)* **15** (2022) 4458. https://doi.org/10.3390/ma15134458

[11] D. G. Stalheim, K. R. Barnes, D. B. Mccutcheon, *International Symposium on Microalloyed Steels for the Oil and gas, Alloy Designs for High Strength Oil and Gas Transmission Linepipe Steels*, United States, 2007, p. 73. https://niobium.tech/-/media/niobiumtech/attachments-biblioteca-tecnica/nt_alloy-designs-for-high-strength-oil-and-gas-transmission-linepipe-steels.pdf

[12] N. Nanninga, A. Slifka, Y. Levy, M. R. Division, C. White, A Review of Fatigue Crack Growth for Pipeline Steels Exposed to Hydrogen, *Journal of Research of the National Institute of Standards and Technology* **115** (2010) 437-452. https://doi.org/10.6028/jres.115.030

[13] D. B. Rosado, W. De Waele, D. Vanderschueren, Latest developments in mechanical properties and metallurgical features of high strength line pipe steels, *International Journal of Sustainable Construction & Design* **4** (2013) 1-10. https://doi.org/10.21825/scad.v4i1.742

[14] J. Luo, L. Zhang, L. Li, F. Yang, W. Ma, K. Wang, X. Zhao, Electrochemical corrosion behaviors of the X90 linepipe steel in NS_4 solution, N*atural Gas Industry B* **3** (2016) 346-351. https://doi.org/10.1016/j.ngib.2016.12.011

[15] J. Luo, S. Luo, L. Li, L. Zhang, G. Wu, L. Zhu, Stress corrosion cracking behavior of X90 pipeline steel and its weld joint at different applied potentials in near-neutral solutions, *Natural Gas Industry B* **6** (2019) 138-144. https://doi.org/10.1016/j.ngib.2018.08.002

[16] H. Bi, J. Miao, C. Ma, C. Zhang, Y. Zhang, Y. Zhou, H. Li, H. Cheng, Combined acoustic emission and electrochemical methods for analyzing the uniform corrosion behavior of X90 high-grade steel pipelines, *Ain Shams Engineering Journal* **16** (2025) 103195. https://doi.org/10.1016/j.asej.2024.103195

[17] M. Yeganeh, M. Omidi, T. Rabizadeh, Anti-corrosion behavior of epoxy composite coatings containing molybdate-loaded mesoporous silica, *Progress in Organic Coatings* **126** (2019) 18-27. https://doi.org/10.1016/j.porgcoat.2018.10.016

[18] M. Yeganeh, I. Khosravi-Bigdeli, M. Eskandari, S. R. A. Zaree, Corrosion Inhibition of L-Methionine Amino Acid as a Green Corrosion Inhibitor for Stainless Steel in the H_2SO_4 Solution, *Journal of Materials Engineering and Performance* **29** (2020) 3983-3994. https://doi.org/10.1007/s11665-020-04890-y

[19] J. M. Reichert, T. Garcin, M. Militzer, W. J. Poole, Formation of Martensite/Austenite (M/A) in X80 Linepipe Steel, 9th International Pipeline Conference, Calgary, Canada, 2012: p. 483. https://doi.org/10.1115/IPC2012-90465

[20] X. X. Dong, Y. F. Shen, Improving mechanical properties and corrosion resistance of 0 . 5 wt.% C TRIP steel by adjusting retained austenite stability and microstructural constituents, *Materials Science and Engineering: A* **852** (2022) 143737. https://doi.org/10.1016/j.msea.2022.143737

[21] C. He, W. Yu, D. Tang, The effect of microstructure on the initial corrosion behavior of low carbon steel in simulated coal solution The effect of microstructure on the initial corrosion behavior of low carbon steel in simulated coal solution, *Materials Research Express* **11** (2024) 056518. https://doi.org/10.1088/2053-1591/ad4cb9

[22] J. M. Zadeh, M. Yeganeh, S. Reza, A. Zaree, M. Khorasanian, Microstructure and corrosion behavior of Ti-10Cu fabricated by selective laser melting, *Materials Today Communications* **39** (2024) 109103. https://doi.org/10.1016/j.mtcomm.2024.109103

[23] M. Yeganeh, M. Saremi, Corrosion inhibition of magnesium using biocompatible Alkyd coatings incorporated by mesoporous silica nanocontainers, *Progress in Organic Coatings* **79** (2015) 25-30. https://doi.org/10.1016/j.porgcoat.2014.10.015

[24] M. Yeganeh, M. T. Shoushtari, P. Jalali, Evaluation of the corrosion performance of selective laser melted 17-4 precipitation hardening stainless steel in Ringer ' s solution, *Journal of Laser Applicatoins* **4** (2021) 042001. https://doi.org/10.2351/7.0000445

[25] M. Yeganeh, A. Keyvani, The effect of mesoporous silica nanocontainers incorporation on the corrosion behavior of scratched polymer coatings, *Progress in Organic Coatings* **90** (2016) 296-303. https://doi.org/10.1016/j.porgcoat.2015.11.006

[26] M. H. Shaeri Karimi, M. Yeganeh, S. R. Alavi Zaree, M. Eskandari, Corrosion behavior of 316L stainless steel manufactured by laser powder bed fusion (L-PBF) in an alkaline solution, *Optics & Laser Technology* **138** (2021) 106918. https://doi.org/10.1016/j.optlastec.2021.106918

[27] S. Mohammadali, J. Moghadas, M. Yeganeh, S. Reza, A. Zaree, M. Eskandari, The influence of heat treatment on the microstructure and corrosion behavior of selective laser melted 316L stainless steel in Ringer's solution, *Surface Topography: Metrology and Properties* **10** (2022) 025012. https://doi.org/10.1088/2051-672X/ac6c42

[28] Z. Shahryari, K. Gheisari, M. Yeganeh, B. Ramezanzadeh, MoO_4^--doped oxidative polymerized pyrrole-graphene oxide core-shell structure synthesis and application for dual-barrier & active functional epoxy-coating construction, *Progress in Organic Coatings* **167** (2022) 106845. https://doi.org/10.1016/j.porgcoat.2022.106845

[29] M. Amirjan, M. Bozorg, H. Sakiani, Investigation of microstructure and corrosion behavior of IN718 superalloy fabricated by selective laser melting, *Materials Chemistry and Physics* **263** (2021) 124368. https://doi.org/10.1016/j.matchemphys.2021.124368
[30] M. Salehi, M. Yeganeh, R. B. Heidari, M. Eskandari, Comparison of the microstructure , corrosion resistance , and hardness of 321 and 310s austenitic stainless steels after thermo-mechanical processing, *Materials Today Communications* **31** (2022) 103638. https://doi.org/10.1016/j.mtcomm.2022.103638
[31] B. Hirschorn, M. E. Orazem, B. Tribollet, V. Vivier, I. Frateur, M. Musiani, Determination of effective capacitance and film thickness from constant-phase-element parameters, *Electrochimica Acta* **55** (2010) 6218-6227. https://doi.org/10.1016/j.electacta.2009.10.065
[32] M. Yeganeh, M. H. Rezvani, S. M. Laribaghal, Electrochemical behavior of additively manufactured 316 L stainless steel in H_2SO_4 solution containing methionine as an amino acid, *Colloids and Surfaces A: Physicochemical and Engineering Aspects* **627** (2021) 127120. https://doi.org/10.1016/j.colsurfa.2021.127120
[33] A. Carmona-Hernandez, R. Orozco-Cruz, E. Mej, A. Espinoza-Vazquez, A. Contreras-Cuevas, R. Galvan-Martinez, Study of SCC of X70 Steel Immersed in Simulated Soil Solution at Different pH by EIS, *Materials (Basel)* **14** (2021) 7445. https://doi.org/10.3390/ma14237445
[34] R. A. Cottis, Interpretation of Electrochemical Noise Data, *Corrosion* **57** (2001) 265-285. https://doi.org/10.5006/1.3290350
[35] Z. Zhang, X. Yuan, Z. Zhao, X. Li, B. Liu, P. Bai, Electrochemical noise comparative study of pitting corrosion of 316L stainless steel fabricated by selective laser melting and wrought, *Journal of Electroanalytical Chemistry* **894** (2021) 115351. https://doi.org/10.1016/j.jelechem.2021.115351
[36] M. Yeganeh, M. T. Shoushtari, A. T. Khanjar, N. H. J. Al Hasan, Microstructure evolution, corrosion behavior, and biocompatibility of Ti-6Al-4V alloy manufactured by electron beam melting (EBM) technique, *Colloids and Surfaces A: Physicochemical and Engineering Aspects* **679** (2023) 132519. https://doi.org/10.1016/j.colsurfa.2023.132519
[37] T. S. N. S. Narayanan, J. Kim, H. W. Park, High performance corrosion and wear resistant Ti-6Al-4V alloy by the hybrid treatment method, *Applied Surface Science* **504** (2019) 144388. https://doi.org/10.1016/j.apsusc.2019.144388
[38] J. Ma, F. Feng, B. Yu, H. Chen, L. Fan, Effect of cooling temperature on the microstructure and corrosion behavior of X80 pipeline steel, *International Journal of Minerals, Metallurgy and Materials* **27** (2020) 347-353. https://doi.org/10.1007/s12613-019-1882-x